ALMOST FIXED QUALITY RATE ALLOCATION
UNDER UNEQUAL SCALING FACTORS
FOR ON-BOARD REMOTE SENSING DATA COMPRESSION

I. Blanes[a†], M. Albinet[b], R. Camarero[b], J. Serra-Sagristà[a]

[a]*Universitat Autònoma de Barcelona, Department of Information and Communications Engineering, Campus UAB, Cerdanyola del Vallès, Spain;* [b]*Centre National d'Études Spatiales, 18 av. Edouard Belin, Toulouse, France*

(*30 December 2016*)

This article extends a rate-allocation method based on the Near-Lossless-Rate (NLR) complexity that is designed to operate on board spacecrafts, to include support for distortion scaling factors, such as those that are needed to code multi- and hyperspectral image when a spectral transform is employed. In this article, the conditions to achieve global minimum distortion are derived under the rate-distortion model based on the NLR complexity for the case of varying distortion scaling factors. Practical implementation issues are dealt with, and a rate-allocation method capable of operating under the constraints of on-board operation is provided. An exhaustive experimental validation of the rate allocation method is performed, reporting modest performances for low rates and close to optimal performances for high rates.

Keywords: on-board data compression; CCSDS-122.0; CCSDS-122.1; hyperspectral images; rate allocation; spectral transforms

1. Introduction

When remote-sensing data is being acquired on board a spacecraft, data compression is an important step to take into account due to, among other considerations, the well-known restrictions on the capacity of the downlink channel, as well as the limited windows of time the channel operates. It is even more relevant when the large volumes of image data generated by multispectral and hyperspectral sensors are considered (see Qian 2013, for a comprehensive review of the field).

A common approach to multi- and hyperspectral data compression is to combine a spectral transform with a regular 2D image coder: first, the spectral transform is applied to the image data, and then each transformed spectral band is encoded with a regular 2D image coder (see Zhang, Fowler, and Liu 2008; Penna et al. 2006a,b, 2007; Fowler and Rucker 2007; Akam Bita, Barret, and Pham 2010; Du, Ly, and Fowler 2014). Such is the case of the draft standard CCSDS-122.1 for multispectral and hyperspectral image data compression being discussed within the Consultative Committee for Space Data Systems (CCSDS), where a spectral transform is applied, and then each resulting transformed image band is independently compressed by a CCSDS-122.0 2D image encoder.

[†]Corresponding author. Email: ian.blanes@uab.cat

Under lossy compression, a scheme such as the previously described requires to vary the rate at which each of the image bands is encoded by CCSDS-122.0 to obtain reasonable coding results. Rate allocation algorithms such as the one described in Camarero, Delaunay, and Thiebaut (2012) and in Bru et al. (2011) are able to address this issue, without requiring modifications to existing space-qualified CCSDS-122.0 hardware and without expensive floating-point operations. However, the spectral transforms in CCSDS-122.1 are designed to limit the dynamic range expansion of the input image after the transform has been applied, and, as a consequence, each transformed image band is, in rough terms, scaled to fit into a limited bit depth. This scaling interferes with the aforementioned rate-allocation algorithms and needs to be taken into account.

This article describes a rate allocation method for high rates, which is based on the Near-Lossless-Rate (NLR) complexity, as described in Camarero, Delaunay, and Thiebaut (2012); Bru et al. (2011), and which supports unequal distortion weighting and thus can be employed in a CCSDS-122.1 encoder.

This paper is organized as follows. The following subsections of this introduction revisit the rate-distortion model based on the NLR complexity and how to employ it for rate allocation. In Section 2, scaling factors are introduced in the model. Subsequently, in Section 3, a rate allocation method employing the described model is proposed. Section 4 presents a comprehensive experimental test of the allocation method. Finally, Section 5 draws some conclusions.

1.1. *Rate-Distortion Model based on the Near-Lossless-Rate Complexity*

A rate-distortion (RD) model relates the distortion introduced in an image coding process with the rate at which the image is coded. These relations are image dependent as they are determined by the amount of information lost during quantization. Thus, as complexities of images being coded vary, so do the relations between rate and distortion.

The RD model based on the NLR complexity, as described in Camarero, Delaunay, and Thiebaut (2012), relates these two magnitudes in function of the *Near-Lossless-Rate* (NLR) image complexity (n.b., in this context the term NLR is unrelated to those coders capable of yielding a bounded peak absolute error). This image complexity is defined as the rate achieved by a transform coder where a constant quantizer with a step size of one is applied after the transform, or more broadly as the rate at which the image is recovered almost losslessly.

For readers convenience, this article follows the same notation and naming conventions as in Camarero, Delaunay, and Thiebaut (2012).

Formally, the RD model based on the NLR complexity relates the rate, R, with the mean squared distortion, MSE, through the image dependent constant, NLR, as follows:

$$R \simeq \text{NLR} - \frac{1}{2} \cdot (\log_2 \text{MSE} + \log_2 12). \tag{1}$$

The NLR RD model is derived from the well-known result from Gish and Pierce (1968):

$$R \simeq H_d(X) - \frac{1}{2} \cdot (\log_2 \text{MSE} + \log_2 12). \tag{2}$$

These theoretical models are derived under many assumptions, i.e., the assumption of a "smooth" PDF, the assumption of an efficient entropy encoder, the assumption of high rate, and the assumption that distortion is invariant at NLR (see Taubman and Marcellin 2002, pp. 105–106). The NLR model is further extended for low rates by using the model described in Falzon and Mallat (1998); however, this extension of the NLR model is left outside the scope of the article.

While Eq. (1) and Eq. (2) are theoretically equivalent, in Camarero, Delaunay, and Thiebaut (2012) and in Bru et al. (2011), it is shown empirically that the relation $\mathrm{NLR} \simeq H_d(X)$ holds true for CCSDS-122.0 and high rate, regardless of the further assumptions that need to be undertaken, such as that CCSDS-122.0 employs a bitplane encoder instead of directly entropy coding quantized coefficients. Moreover, through our experimental results, it will be shown that this model is also applicable when the 2D Integer Discrete Wavelet Transform (Integer DWT) is employed in CCSDS-122.0 and no quantization is applied before the bitplane encoder.

1.2. *Optimal Rate Allocation*

The NLR-based RD model can be employed to provide almost fixed quality encodings for an image, by knowing at which rate it has to be coded to achieve a certain distortion. In addition, it can also be employed to unevenly allocate rate within an image.

Let S be the number of segments (regions) in which an image is partitioned for the purposes of rate allocation (e.g., S may be the number of segments of a CCSDS-122.0 bitstream) and let $0 \leq s < S$. Following Eq. (1), for each segment,

$$R_s \simeq \mathrm{NLR}_s - \frac{1}{2} \cdot (\log_2 \mathrm{MSE}_s + \log_2 12). \tag{3}$$

To allocate a total rate of $R > 0$ among all S segments, with a rate R_s for each segment, the optimal rate-allocation problem can be formulated as

$$\underset{R_0,...,R_{S-1}}{\mathrm{argmin}} \sum_{s=0}^{S-1} MSE_s(R_s) \qquad \text{s.t.} \qquad R = \sum_{s=0}^{S-1} R_s. \tag{4}$$

It is well known that this can be solved through the method of Lagrange multipliers, which yields the following necessary conditions for a solution of the preceding optimization problem.

$$\frac{\partial}{\partial R_{\hat{s}}} \left(\sum_{s=0}^{S-1} MSE_s(R_s) - \lambda \left(R - \sum_{s=0}^{S-1} R_s \right) \right) = 0, \quad 0 \leq \hat{s} < S. \tag{5}$$

Eq. (3) can be reformulated as

$$\mathrm{MSE}_s \simeq \frac{1}{12} \cdot 2^{2(\mathrm{NLR}_s - R_s)}. \tag{6}$$

Substituting Eq. (6) into Eq. (5) and differentiating yields

$$\lambda = \frac{1}{6} 2^{2(\mathrm{NLR}_{\hat{s}} - R_{\hat{s}})} \cdot \ln(2), \tag{7}$$

which can be rearranged as

$$\frac{\lambda}{2\ln(2)} = \frac{1}{12}2^{2(\mathrm{NLR}_{\hat{s}} - R_{\hat{s}})} = MSE_{\hat{s}}(R_{\hat{s}}). \tag{8}$$

Hence, it is a necessary condition that $MSE_i(R_i) = MSE_j(R_j)$ for $0 \leq i, j < S$. Or in other words, it is necessary that all segments have equal distortion to obtain minimum global distortion, under the RD model of Eq. (1). Hence, this solution provides theoretically uniform levels of image quality (in terms of MSE) for all image bands.

Having $MSE_s(R_s)$ equal for all s yields the following solution to the rate allocation problem:

$$R_s = \mathrm{NLR}_s - C. \tag{9}$$

Since $R = \sum_{s=0}^{S-1} R_s$,

$$C = \frac{\sum_{s=0}^{S-1} \mathrm{NLR}_s - R}{S}. \tag{10}$$

Variable C is constrained to $0 \leq C \leq \mathrm{NLR}_s$ which is not usually a problem to satisfy. Setting $R \leq \sum_{s=0}^{S-1} \mathrm{NLR}_s$ guarantees $C \geq 0$ and that R_s is below the maximum rate achievable of NLR_s. Having R high enough so that $C \leq \min\{\mathrm{NLR}_s\}$ ensures that the allocated rate for a segment is not negative (i.e., $R \geq \sum_{s=0}^{S-1} \mathrm{NLR}_s - S \cdot \min\{\mathrm{NLR}_s\}$). These constraints that restrict the NLR-based model to high enough rates will be lifted in further sections.

There is one additional matter regarding this rate allocation model. The number of segments S of an image may not be well defined in an scenario where a pushbroom sensor generates an "infinite" image as the sensor displaces. In this case, it may be necessary to apply the rate-allocation method at regular time intervals among the newly acquired segments as if they were all the segments of a new image.

2.   Unequal Scaling Factors

2.1.   *Scaling Factors*

Scaling factors are often established to weight the distortion contribution of particular image segments, such when it is desired that a particular zone of an image is recovered with a higher fidelity. A common case where scaling factors are needed is when coding transforms are employed for the purposes of preserving Parseval's identity.

Similarly as before, let S be the number of segments in which a transformed image is partitioned for the purposes of rate allocation (in this occasion, allocation is performed on the transformed domain) and let $0 \leq s < S$. For simplicity and without loss of generality during the description of the model, it can be assumed that each segment is one of the "bands" of the transformed image.[1]

---

[1]N.b., the term band is a misnomer employed here to denote a component resulting from a spectral transform. After a spectral transform a band no longer corresponds to a frequency band in the spectral domain.

For transforms preserving Parseval's identity, such as the Discrete Cosine Transform or Karhunen-Loeve Transform, it can be seen that distortion contributions measured within the transformed domain, $\mathrm{MSE}'_s(R_s)$, directly translate to the recovered image. For these cases, rate can be allocated in the transformed domain as described before by substituting $\mathrm{MSE}_s(R_s)$ by $\mathrm{MSE}'_s(R_s)$ in Eq. (5).

There are other instances where transforms produce signals which are approximately ξ_s times smaller than would be for an equivalent transform that preserved Parseval's identity, such as the common implementation of the Integer Wavelet Transform (IWT) described in Gall and Tabatabai (1988), or the Pairwise Orthogonal Transform (POT) in its isorange variant described in Blanes et al. (2015).

In such instances, distortion introduced in the transformed domain is modeled as

$$\mathrm{MSE}_s(R_s) \simeq \xi_s^2 \cdot \mathrm{MSE}'_s(R_s), \tag{11}$$

with MSE'_s being measured in the transformed domain, and $\mathrm{MSE}_s(R_s)$ being the equivalent distortion contribution of segment s into the total MSE (even if it is now spread by the transform over all the recovered image). Scaling factors ξ_s are determined by the transform employed, being usually the norm of the synthesis basis vectors. Note that for spectral transforms, scaling factors ξ_s are constant for all segments within the same transformed bands.

2.2. Rate-Distortion Model

The relation of Eq. (3) is not altered by prepending a coding transform to an image coder, provided that the underlying assumptions stated previously are preserved. In this case, rate and distortion in the transformed domain can be related as

$$R_s \simeq \mathrm{NLR}_s - \frac{1}{2} \cdot \left(\log_2 \mathrm{MSE}'_s + \log_2 12 \right). \tag{12}$$

The previous equation can be extended with the inclusion of scaling factors from Eq. (11) to relate rate with the MSE in the original domain as

$$R_s \simeq \mathrm{NLR}_s - \frac{1}{2} \cdot \left(\log_2 \left(\frac{\mathrm{MSE}_s}{\xi_s^2} \right) + \log_2 12 \right). \tag{13}$$

This can be reformulated as

$$R_s \simeq \mathrm{NLR}_s + \log_2 \xi_s - \frac{1}{2} \cdot \left(\log_2 \mathrm{MSE}_s + \log_2 12 \right), \tag{14}$$

and as

$$\mathrm{MSE}_s \simeq \frac{1}{12} \cdot 2^{2(\mathrm{NLR}_s + \log_2 \xi_s - R_s)}. \tag{15}$$

As before, applying the method of lagrange multipliers yields a solution with a constant $MSE_s(R_s)$ of

$$\frac{\lambda}{2 \ln(2)} = \frac{1}{12} 2^{2(\mathrm{NLR}_{\hat{s}} + \log_2 \xi_{\hat{s}} - R_{\hat{s}})} = MSE_{\hat{s}}(R_{\hat{s}}), \tag{16}$$

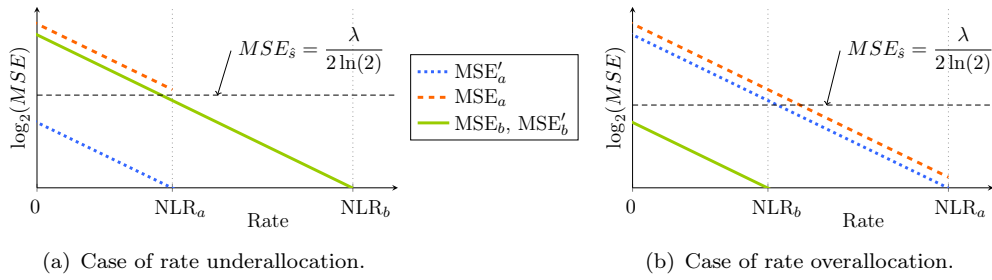(a) Case of rate underallocation. (b) Case of rate overallocation.

Figure 1.: Rate allocation issues.

and the rate allocation problem can now be solved as

$$R_s = \text{NLR}_s + \log_2 \xi_s - C, \tag{17}$$

with a trivial solution of

$$C = \frac{\sum_{s=0}^{S-1} \text{NLR}_s + \sum_{s=0}^{S-1} \log_2 \xi_s - R}{S} \tag{18}$$

for a given $R = \sum_{s=0}^{S-1} R_s$.

However, in this case the value C is constrained to

$$\log_2 \xi_s \leq C \leq \text{NLR}_s + \log_2 \xi_s, \tag{19}$$

which is often hard to satisfy for all s. More so considering that $\log_2 \xi_s$ may take positive and negative values.

3. Rate Allocation Strategy

3.1. *Constrained Solution*

The trivial solution presented in Eq. (18) can be difficult to achieve in practice. Suppose that rate is split between two segments a and b, with $\xi_a > 1$ and $\xi_b = 1$. As per Eqs. (12) and (14), the MSE relations depicted in Fig. 1 can occur.

The largest rate the encoders can reach for segment a and b is by definition NLR_a and NLR_b respectively, and hence, for the compressed image is $\text{NLR}_a + \text{NLR}_b$. However, in the case of Fig. 1(a), for a total rate R just over $\text{NLR}_a + \text{NLR}_b - \log_2(\xi_a)$, the trivial solution of Eq. 18 targets a non-achievable constant $MSE_{\hat{s}}$, as R_a needs to be larger than NLR_a, i.e., the rate for segment a needs to be over what can be provided. A more sensible solution would be to limit R_a to NLR_a and allocate the remaining rate to R_b, which would still decrease overall distortion.

Similarly, the relation shown in Fig. 1(b) may also occur. In this case, for a total rate R smaller than $\text{NLR}_a - \text{NLR}_b + \log_2(\xi_a)$, the trivial solution of Eq. 18 targets a non-achievable constant $MSE_{\hat{s}}$, as the resulting R_b is smaller than 0. This results in rate over allocation because $R_a = R - R_b$ and thus $R_a > R$. A more sensible solution would be to limit R_b to be at least 0 and not allocate additional rate to R_a.

In practice, Eq. (17) can be turned into the following monotonically increasing function of C' that saturates for values outside achievable rates (below 0 and over
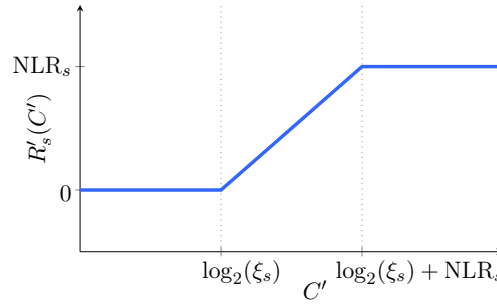
Figure 2.: Plot of $R_s'(C')$.

NLR_s), as depicted in Fig. 2.

$$R_s'(C') = \begin{cases} 0, & C' < -\mathrm{NLR}_s - \log_2(\xi_s) \\ \mathrm{NLR}_s, & -\log_2(\xi_s) < C' \\ \mathrm{NLR}_s + \log_2(\xi_s) + C', & \text{otherwise} \end{cases} \tag{20}$$

While the trivial solution of Eq. (18) is not applicable to solve

$$R = \sum_{s=0}^{S-1} R_s'(C'), \tag{21}$$

functions $\left\{ R_s'(C') \right\}$ are monotonically increasing, and thus $\sum_{s=0}^{S-1} R_s'(C')$ is a monotonically increasing function as well, which is suitable to be easily solved (for example by a bisection algorithm). Thus, by modeling the total rate as a summation of monotonically increasing functions, the NLR-based model can be employed for the case of unequal scaling factors.

Interestingly, the process of obtaining the NLR-based model for unequal scaling factors, has yielded one additional corollary: the restrictions on high-enough rate that are stated on the last paragraph of section 1.2 are now lifted, and the NLR-based model can be employed at any desired rate.

3.2. *Implementation*

A method to solve Eq. (21) for any $0 \leq R \leq \sum_{s=0}^{S-1} \mathrm{NLR}_s$ is now described. The method iterates over variable C_i' until $R = \sum_{s=0}^{S-1} R_s'(C_i')$ is achieved. Since any increase in C_i' is bounded to obtain at most S times such an increase in $\sum_{s=0}^{S-1} R_s'(C_i')$, at each iteration, C_i' is increased by the amount of rate needed to reach R from $\sum_{s=0}^{S-1} R_s'(C_{i-1}')$ divided by S.

The method operates as follows:

Step 1 For $i = 0$, initialize C_0' with a sufficiently small value so that $\sum_{s=0}^{S-1} R_s'(C_0') \leq 0$. I.e., $C_0' \leq -\max\left\{\mathrm{NLR}_s + \log_2(\xi_s)\right\}$.

Step 2 Find $\Delta_i = \dfrac{R - \sum_{s=0}^{S-1} R_s'(C_i')}{S}$.

Step 3 Obtain C_{i+1}' as $C_{i+1}' = C_i' + \Delta_i$.

Step 4 If $\Delta_i > 0$, increase i by 1 and proceed to **Step 2**.

Applying this method achieves $R = \sum_{s=0}^{S-1} R_s'(C_i')$. If needed, convergence can be speeded up in step 2 by dividing by the number of segments where $R_s'(C_i') < \mathrm{NLR}_s$

instead of by S.

   While this algorithm is described in units of bits per pixel, in practice R could be measured in bytes (per file). In this case, the terms $\log_2(\xi_s)$ of Eq. (20) need to be scaled by the number of samples per band, and Δ_i should be rounded down after step 2. The algorithm is then guaranteed to provide at most a difference of $S - 1$ bytes between R and $\sum_{s=0}^{S-1} R'_s(C'_i)$, which can be addressed by adding one extra byte to rates R'_s for bands where $s < R - \sum_{s=0}^{S-1} R'_s(C'_i)$.

   Note well that given the large number of different root-finding algorithms capable of solving $R - \sum_{s=0}^{S} R'_s(C') = 0$, it is likely that an interested implementer will apply an algorithm better suited to their on-board hardware. This algorithm is a simple indication of how this can be solved, without further constraints on efficiency or the amount of iterations needed to converge.

4.   Experimental Results

This section reports on an exhaustive validation of the NLR model. The NLR rate-allocation method, as is the case with most model-based allocation methods, is expected to produce varying results whenever images characteristics diverge from those expected by the model. Moreover, satellite-acquired images usually present varied artifacts that further difficult the rate allocation process (e.g., streaking artifacts, shot noise, or dead pixels). As such, the performance of the NLR needs to be analyzed under a wide array of circumstances.

4.1.   *Experimental Setup*

For the purpose of evaluating on-board image compression methods, the Multi-specral Hyperspectral Data Compression (MHDC) Working Group of the CCSDS has collected a corpus of images from different instruments and missions[2]. In this article a varied subset of 24 images from 14 different instruments is employed, with images from multi- and hyperspectral instruments, as well as images from infrared sounder instruments. The corpus includes images of varying dimensions, resolution (both spatial and spectral resolutions), and bit depth. Moreover, the corpus includes data as captured by the sensor (L0 data), which has strong noise and artifacts that are only addressed on the ground. Details of the images selected are reported in Table 1.

   The rate-allocation method described in this document has been tested in combination with CCSDS-122.1 (as specified in the latest draft available in 2016). The image encoder has been configured using the parameters values indicated in Table 2. The number of *Blocks Per Segment* is set so that no intra-band rate allocation is performed; i.e., within the same band no rate allocation is performed, and the default coefficient scan order of CCSDS-122.0 is employed to provide varying rates and qualities. Whilst outside the scope of this article, the NLR method can be employed to perform intra-band rate allocation, which improves compression performance at the cost of larger on-board memory buffers.

   In order to evaluate different scaling factors, two of the three available transforms in CCSDS-122.1 have been tested; namely the IWT and the POT. The third transform available in CCSDS-122.1, an Arbitrary Affine Transform, is supported

---

[2]Publicly available at `http://cwe.ccsds.org/sls/docs/SLS-DC/123.0-B-Info/TestData`.

Table 1.: Technical details of the subset of the MHDC-CCSDS corpus. Images are unsigned unless their bit depth is marked with a ‡. NUC stands for (simulated on-board) non-uniformity correction.

Name	Type	Bands	Height	Width	Bit Depth
AIRS-Granule-9	raw	1501	135	90	13
AVIRIS-Hawaii-raw	raw	224	512	614	10
AVIRIS-Yellowstone-rad	radiance	224	512	677	14‡
AVIRIS-Yellowstone-raw	raw	224	512	680	15
CASI-t0477f06-nuc	nuc	72	1225	406	13
CASI-t0477f06-raw	raw	72	1225	406	12
CRISM-sc214-nuc	nuc	74	2700	64	11
CRISM-sc214-raw	raw	74	2700	64	11
Hyperion-GeoSample-ff	flatfielded raw	242	1024	256	13‡
Hyperion-GeoSample-nuc	nuc	242	1024	256	12
Hyperion-GeoSample-raw	raw	242	1024	256	12
IASI-Desert	calibrated	8461	60	66	12
Landsat-Coast	raw	6	1024	1024	8
Landsat-Mountain	raw	6	1024	1024	8
M3-globalA-nuc	nuc	86	512	320	11
M3-globalA-raw	raw	86	512	320	12
MODIS-250m-raw	raw	2	8120	5416	12
MODIS-500m-raw	raw	5	4060	2708	12
MSG-RC15	calibrated	11	3712	3712	10
Pleiades-Montpellier	HR, simulated	4	2456	224	12
SFSI-Mantar-rad-rmnoise	noise-filtered radiance	240	140	452	16‡
SFSI-Mantar-raw	raw	240	140	496	11
SPOT5-Toulouse-1	HRG, processed	3	1024	1024	8
VEGETATION-1-1c	raw	4	10080	1728	10

Table 2.: Parameters employed for the CCSDS-122.1 image encoder.

Parameter	Value
Segments per Band (per Region)	1
Upshift	0
Downshift	0
Output Word Size	1
Spectral Transform	IWT, POT
Blocks Per Segment (S)	Max. possible
OptDCSelect and OptACSelect	Optimal
2D DWT	Integer DWT, Float DWT
Custom Sub-band weights	No
Region Size (F)	8
Ω	11
Flip Mode	Stable

as well by the method described in this article, but no experimental results have been performed as the unequal scaling factors for this transform are user-defined.

Results are compared with two other rate-allocation methods. The first method is the Reverse Water-filling (RW) method, which employs a model similar to the one described in this document but where the variance of the input is used instead of the NLR complexity (a description of the method can be found in section 5.2 of Taubman and Marcellin 2002). As with the NLR method, wrong rate allocations may occur with the RW method (it may produce negative rates for segments where no rate should be allocated, increasing the total amount of rate allocated). For

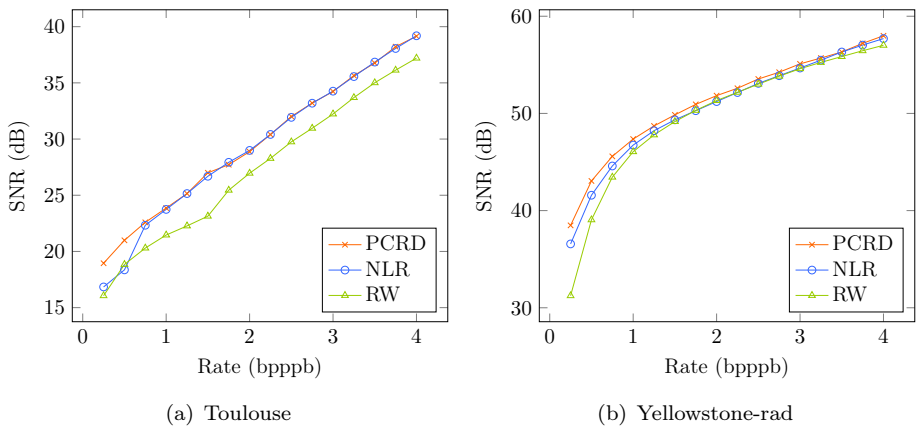(a) Toulouse   (b) Yellowstone-rad

Figure 3.: Results for the Toulouse and Yellowstone-rad images.

the RW method, this has been addressed by setting a minimum per-segment rate, and proportionally reducing the rate of segments with positive rates whenever rate overallocation occurs. The second rate-allocation method is the Post-Compression Rate-Distortion (PCRD) optimization method, which yields quasi-optimal performance by applying the method of the lagrange multipliers to the convex hull of the actual RD curves. The PCRD method requires accurate measurements of distortion to be provided while an image is being coded to obtain the RD curves, and thus requires changes to existing CCSDS-122.0 hardware.

4.2. *Experimental data*

First, some basic experimental results are reported that establish the major trends of the experimental data, and afterwards, detailed experimental data is provided.

Rate allocation curves are reported in Fig. 3 for two images from the CCSDS MHDC corpus: the SPOT5-Toulouse-1 image and the AVIRIS-Yellowstone-rad image. The IWT has been employed for the Toulouse image and the POT has been employed for the Yellowstone-rad image, and for both images the Float DWT is employed in CCSDS-122.0. Results are reported in terms of Signal-to-Noise (SNR)[3], in dB, in relation to rate, in bits per pixel per band (bpppb). As expected, results of the PCRD method are better than those of the NLR or RW methods. For the Toulouse image, NLR virtually provides the same results as PCRD, except at rates below 0.75 bpppb, where a noticeable difference occurs. For the Yellowstone-rad image, NLR provides results between those of the PCRD and RW methods, with the NLR and RW methods yielding significantly lower performances than the PCRD method at low rates.

In Fig. 4, the actual distribution of rate for each band is reported when coding the image Yellowstone at 1 bpppb. All rate allocation methods present similar allocations for each band of the transformed image. The figure reports the expected outcome of a spectral transform, where most the energy is accumulated in the first bands of a transformed image. Performance variations in Fig. 3(b) are explained by small variations in the rates reported in Fig. 4.

While the previous plots may suggest trends in rate allocation performance, ex-

---

[3]SNR is here computed based on the energy of the input signal as $10 \cdot \log_{10} \left(\sum (I_{i,j,k})^2 / \sum (I_{i,j,k} - \hat{I}_{i,j,k})^2 \right)$, being I the original image and $\hat{I}$ the recovered image.
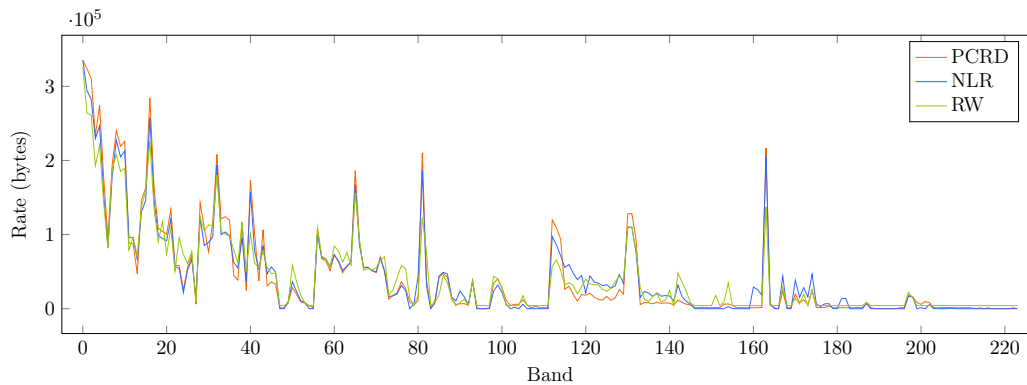
10

Figure 4.: Rate distribution for the image Yellowstone at 1 bpppb.

haustive experimental results have been performed to further assess the performance of the described method. These experimental results have been designed to cover 288 different combinations of factors that may affect rate allocation: 24 images have been tested, for both the IWT and POT spectral transforms, for both the Integer and Float DWTs in CCSDS-122.0, and at rates of 1, 2 and 3 bpppb.

For each combination of factors, experimental results are reported either in terms of SNR for the NLR method, or both in terms of the SNR difference over the NLR method and in terms of the percentage of additional rate needed to match the SNR of the NLR method. In order to obtain the mentioned percentage of additional rate, coding performance for the RW and PCRD methods has been sampled at intervals of 0.002 bpppb to find the rate for which SNR results matched those of the NLR method.

Tables 3 and 4 report on the experimental results where the Float DWT is employed in CCSDS-122.0 and where the IWT and the POT are employed as spectral transforms. While rate allocation results vary significantly as expected for a corpus of satellite images, a clear difference can be made between results at low and high rates. Quality-wise, the penalties between the quasi-optimal PCRD method and the other two model-based methods range from very large at low rates, to moderate and small at high rates.

At 1 bpppb, there is a large disparity between the performance of the methods. When compared with the PCRD method, the NLR and RW methods consistently and significantly underperform, with PCRD requiring up to 10 times less rate to achieve the same quality on some cases. The RW and particularly the NLR methods perform very poorly when the IWT is employed, which may be attributed to the lower energy concentration provided by the IWT transform. These results are expected as the extended non-linear NLR model for low rates is not being used.

The volatility and low performance present at 1 bpppb recede as the rate employed transitions into to higher rate regions. At 2 bpppb, the NLR method consistently outperforms the RW method and reaches a SNR performance of about 0.5 dB less than that of the PCRD method. At 3 bpppb, results between NLR and PCRD are very close. Again, as expected from a corpus of satellite images, a couple of low-performing cases remain (the IASI image for the IWT and the MODIS-500m-raw image for the POT), but overall the PCRD method only requires about 4% less rate to achieve the same quality as the NLR method.

It is also worth mentioning that there are a couple of instances where PCRD is a bit worse than the other allocation methods (e.g., requiring 1 or 2 percent more rate to achieve the same quality as the NLR method). This may be attributed to non-exact distortion measures caused by rounding errors within the transforms that

Table 3.: Performance of the NLR rate-allocation method in comparison with the RW and PCRD methods, when employing the IWT spectral transform and the Float DWT spatial transform.

Image Name	1 bpppb			2 bpppb			3 bpppb		
	NLR (dB)	RW (Δ dB, %)	PCRD (Δ dB, %)	NLR (dB)	RW (Δ dB, %)	PCRD (Δ dB, %)	NLR (dB)	RW (Δ dB, %)	PCRD (Δ dB, %)
AIRS-Granule-9	39.94	14.25 −78%	15.93 −90%	59.59	−1.44 +22%	0.52 −7%	63.38	−2.04 +21%	0.38 −3%
AVIRIS-Hawaii-raw	40.09	4.65 −46%	5.67 −69%	48.12	−0.24 +6%	0.78 −10%	51.36	−1.75 +35%	0.40 −2%
AVIRIS-Yellowstone-rad	39.81	1.95 −18%	5.05 −47%	49.97	−1.38 +16%	0.63 −7%	54.06	−1.39 +13%	0.48 −5%
AVIRIS-Yellowstone-raw	37.59	6.33 −43%	9.16 −61%	43.79	8.07 −51%	9.75 −63%	58.01	−1.57 +13%	0.39 −3%
CASI-t0477f06-raw	36.54	4.68 −32%	6.24 −49%	48.28	−0.15 +2%	0.32 −3%	52.55	−0.58 +5%	0.39 −3%
CASI-t0477f06-raw-nuc	36.55	4.77 −32%	6.37 −49%	48.41	−0.16 +2%	0.37 −4%	52.65	−0.58 +5%	0.39 −3%
CRISM-sc214-nuc	39.32	4.26 −41%	10.89 −83%	55.43	−6.83 +70%	0.50 −6%	58.79	−5.59 +36%	0.63 −4%
CRISM-sc214-raw	27.74	3.01 −38%	13.16 −77%	48.57	−5.75 +25%	2.38 −13%	55.99	−2.95 +19%	0.47 −5%
Hyperion-GeoSample-ff	24.30	−0.19 +5%	0.29 −8%	28.13	−0.53 +7%	0.37 −4%	31.91	−0.67 +7%	0.15 −2%
Hyperion-GeoSample-raw	39.90	1.16 −20%	3.95 −50%	48.04	−1.85 +20%	0.73 −9%	52.65	−2.13 +19%	0.27 −3%
Hyperion-Geo_Sample-nuc	45.00	0.06 −2%	1.32 −27%	49.93	−1.62 +24%	0.38 −4%	53.94	−2.23 +22%	0.28 −3%
IASI-Desert	35.12	10.71 −83%	12.45 −90%	43.51	5.30 −68%	9.16 −81%	52.91	−1.12 +10%	4.07 −32%
Landsat-Coast	37.08	−0.69 +23%	−0.03 +1%	39.78	−0.76 +12%	0.28 −3%	44.67	−3.14 +41%	−0.01 +0%
Landsat-Mountain	26.15	−0.01 +0%	0.36 −10%	30.87	−0.34 +4%	0.14 −3%	34.30	−0.72 +8%	0.47 −4%
M3-M3globalA-nuc	53.09	−4.11 +48%	1.83 −28%	59.03	−3.63 +29%	0.39 −2%	61.88	−1.52 +23%	0.41 −6%
M3-M3globalA-raw	40.10	−3.44 +22%	4.43 −34%	54.45	−2.21 +10%	0.64 −4%	59.66	−0.69 +8%	0.38 −4%
MODIS-250m-raw	33.88	−1.59 +11%	−0.23 +2%	41.32	−0.07 +0%	0.43 −3%	47.55	0.25 −1%	0.52 −2%
MODIS-500m-raw	20.16	4.56 −75%	9.90 −89%	34.41	−7.78 +20%	2.25 −20%	42.62	−3.44 +18%	0.00 0%
MSG-RC15	29.12	6.71 −65%	10.67 −81%	45.62	−4.32 +30%	0.06 −1%	49.52	−1.80 +16%	0.30 −2%
Pleiades-Montpellier	22.35	4.73 −60%	7.67 −72%	36.60	−2.75 +15%	0.01 0%	42.15	−1.40 +9%	0.45 −2%
SFSI-Mantar-rad-rmnoise	39.19	4.99 −32%	10.32 −71%	54.49	−1.49 +14%	1.54 −14%	59.46	−2.02 +21%	0.67 −5%
SFSI-Mantar-raw	37.12	−0.50 +20%	0.27 −9%	40.72	−1.24 +15%	0.28 −4%	45.61	−2.28 +14%	0.16 −2%
SPOT5-Toulouse-1	23.74	−2.28 +55%	0.12 −3%	28.99	−2.03 +18%	−0.11 +1%	34.26	−2.03 +12%	−0.03 +0%
VEGETATION-1-1c	34.58	−0.77 +6%	0.77 −10%	41.92	−0.55 +4%	0.06 −1%	47.35	−0.51 +3%	0.00 0%

yield the similar, but not equal, relation in Eq. (11).

Tables 5 and 6 report on the experimental results where the Integer DWT is employed in CCSDS-122.0 and where the IWT and the POT are employed as spectral transforms. Overall, the experimental results are in line with those for the Float DWT, and show that the NLR model holds as well for the Integer DWT even if the coefficients after the 2D wavelet transform are not quantized as expected by the theoretical model under the assumptions stated in Section 1.1 (these coefficients are already integer values suitable for bitplane encoding). At high rates, where the NLR model performs well, employing the Integer DWT further closes the gap between the NLR model and the PCRD to 2% or less in most cases.

Table 4.: Performance of the NLR rate-allocation method in comparison with the RW and PCRD methods, when employing the POT spectral transform and the Float DWT spatial transform.

Image Name	1 bpppb			2 bpppb			3 bpppb		
	NLR (dB)	RW (Δ dB, %)	PCRD (Δ dB, %)	NLR (dB)	RW (Δ dB, %)	PCRD (Δ dB, %)	NLR (dB)	RW (Δ dB, %)	PCRD (Δ dB, %)
AIRS-Granule-9	57.34	−0.13 +4%	0.47 −11%	60.63	−0.30 +5%	0.47 −8%	63.76	−0.50 +6%	0.27 −3%
AVIRIS-Hawaii-raw	45.72	0.24 −9%	0.66 −29%	48.21	−0.11 +3%	0.57 −10%	50.69	−0.83 +20%	−0.01 +0%
AVIRIS-Yellowstone-rad	46.74	−0.68 +9%	0.62 −8%	51.22	0.10 −1%	0.61 −8%	54.67	−0.07 +1%	0.43 −4%
AVIRIS-Yellowstone-raw	51.01	−0.73 +10%	0.53 −6%	55.88	−0.18 +2%	0.45 −5%	60.70	−0.47 +3%	0.21 −2%
CASI-t0477f06-raw	40.76	0.62 −7%	2.39 −27%	47.99	−0.74 +9%	0.44 −5%	52.19	−0.98 +9%	0.19 −2%
CASI-t0477f06-raw-nuc	43.08	−1.28 +15%	0.74 −10%	48.52	−0.82 +10%	0.47 −6%	52.58	−0.98 +9%	0.45 −3%
CRISM-sc214-nuc	49.14	−0.08 +1%	2.38 −33%	55.59	−0.34 +4%	0.62 −9%	58.30	−0.51 +9%	0.30 −5%
CRISM-sc214-raw	39.06	1.19 −11%	3.04 −22%	50.53	−1.77 +22%	0.83 −6%	55.52	−2.82 +18%	0.41 −5%
Hyperion-GeoSample-ff	25.17	0.06 −2%	0.63 −14%	28.56	0.01 −0%	0.66 −9%	31.87	−0.36 +4%	0.14 −2%
Hyperion-GeoSample-raw	42.77	0.37 −5%	1.73 −25%	49.04	−0.46 +6%	0.55 −6%	52.84	−0.40 +4%	0.35 −3%
Hyperion-Geo_Sample-nuc	46.52	−0.29 +6%	0.53 −12%	50.54	−0.33 +4%	0.45 −7%	54.06	−0.37 +4%	0.28 −4%
IASI-Desert	46.33	0.14 −3%	1.13 −22%	51.16	−0.37 +4%	0.67 −9%	55.41	−0.68 +6%	0.28 −2%
Landsat-Coast	36.93	−0.28 +14%	0.33 −14%	39.80	−0.85 +15%	0.22 −2%	44.08	−2.73 +54%	−0.01 +0%
Landsat-Mountain	27.34	−0.22 +4%	0.24 −4%	31.37	0.20 −3%	0.53 −6%	35.01	−0.22 +3%	0.02 −0%
M3-M3globalA-nuc	54.46	−1.90 +30%	0.56 −11%	58.27	−0.43 +8%	0.32 −7%	60.93	−0.69 +15%	0.04 −1%
M3-M3globalA-raw	40.50	0.56 −3%	5.01 −38%	54.51	−1.12 +8%	0.70 −3%	59.13	−1.09 +14%	0.28 −4%
MODIS-250m-raw	23.62	11.63 −84%	12.92 −86%	44.15	−1.09 +5%	0.14 −1%	51.06	−0.73 +4%	0.02 −0%
MODIS-500m-raw	29.19	−2.91 +28%	0.80 −9%	36.17	0.50 −5%	2.17 −16%	38.91	4.08 −22%	6.09 −31%
MSG-RC15	32.18	6.53 −70%	8.74 −73%	46.41	−3.47 +32%	0.36 −3%	49.81	−1.09 +10%	0.51 −6%
Pleiades-Montpellier	29.32	0.18 −3%	0.34 −5%	36.57	−0.30 +2%	0.17 −1%	42.11	−0.19 +1%	0.41 −3%
SFSI-Mantar-rad-rmnoise	50.39	−0.67 +7%	0.75 −10%	56.03	−0.26 +4%	0.27 −5%	58.88	−0.45 +7%	0.38 −3%
SFSI-Mantar-raw	37.56	−0.11 +4%	0.23 −8%	41.43	−0.56 +6%	0.35 −4%	46.02	−1.00 +7%	−0.01 +0%
SPOT5-Toulouse-1	25.35	0.85 −11%	0.95 −15%	31.96	−0.04 +0%	0.09 −1%	36.63	−0.02 +0%	0.11 −1%
VEGETATION-1-1c	33.88	0.12 −2%	2.47 −29%	42.74	−0.62 +6%	0.14 −1%	47.92	−0.57 +4%	−0.07 +0%

Table 5.: Performance of the NLR rate-allocation method in comparison with the RW and PCRD methods, when employing the IWT spectral transform and the Integer DWT spatial transform.

Image Name	1 bpppb			2 bpppb			3 bpppb		
	NLR (dB)	RW (Δ dB, %)	PCRD (Δ dB, %)	NLR (dB)	RW (Δ dB, %)	PCRD (Δ dB, %)	NLR (dB)	RW (Δ dB, %)	PCRD (Δ dB, %)
AIRS-Granule-9	40.00	14.05 −78%	15.24 −90%	58.69	−0.79 +12%	0.53 −8%	62.27	−1.22 +12%	0.23 −2%
AVIRIS-Hawaii-raw	40.18	3.65 −42%	4.48 −62%	47.18	0.33 −5%	0.66 −8%	52.16	−1.71 +18%	−0.41 +2%
AVIRIS-Yellowstone-rad	39.63	2.53 −21%	4.61 −45%	48.93	−0.25 +3%	0.68 −9%	52.81	−0.24 +2%	0.56 −4%
AVIRIS-Yellowstone-raw	37.62	6.48 −42%	8.81 −60%	43.72	8.33 −51%	9.40 −62%	57.19	−0.79 +7%	0.50 −4%
CASI-t0477f06-raw	36.46	4.29 −33%	5.99 −47%	47.57	−0.22 +2%	0.34 −4%	51.56	−0.14 +1%	0.36 −3%
CASI-t0477f06-raw-nuc	36.47	4.44 −34%	6.05 −48%	47.68	−0.24 +3%	0.46 −4%	51.64	−0.16 +2%	0.34 −3%
CRISM-sc214-nuc	39.40	5.27 −47%	10.07 −81%	54.58	−5.11 +41%	0.47 −5%	58.62	−3.18 +19%	0.58 −2%
CRISM-sc214-raw	27.83	5.65 −56%	12.64 −76%	49.25	−3.38 +18%	0.80 −5%	55.05	−2.37 +17%	0.35 −4%
Hyperion-GeoSample-ff	23.69	0.08 −2%	0.28 −9%	27.18	0.00 −0%	0.19 −3%	30.91	−0.20 +2%	0.10 −0%
Hyperion-GeoSample-raw	40.05	1.04 −17%	3.35 −45%	47.75	−1.16 +13%	0.37 −5%	51.59	−0.97 +9%	0.17 −2%
Hyperion-Geo_Sample-nuc	44.69	0.11 −3%	1.11 −23%	49.17	−0.86 +12%	0.30 −4%	52.97	−1.13 +10%	0.15 −1%
IASI-Desert	35.04	10.62 −84%	12.04 −91%	43.53	5.69 −69%	8.27 −80%	53.31	−0.39 +3%	2.46 −21%
Landsat-Coast	35.96	−0.14 +5%	0.05 −2%	39.11	−0.58 +8%	−0.05 +1%	47.31	−5.50 +29%	0.71 −1%
Landsat-Mountain	25.50	0.20 −3%	0.31 −9%	29.77	0.44 −4%	0.08 −1%	33.32	−0.24 +3%	0.07 −1%
M3-M3globalA-nuc	53.65	−2.68 +53%	0.28 −6%	58.52	−2.07 +16%	0.23 −2%	64.72	−3.07 +18%	−0.25 +1%
M3-M3globalA-raw	41.16	−3.27 +23%	3.18 −25%	53.73	−1.45 +9%	0.24 −2%	59.02	−1.11 +10%	0.25 −2%
MODIS-250m-raw	33.59	−1.26 +11%	−0.19 +2%	40.98	−0.02 +0%	0.41 −3%	46.95	0.28 −2%	0.24 −2%
MODIS-500m-raw	20.13	4.84 −77%	9.98 −89%	34.31	0.51 −3%	2.30 −21%	42.20	−1.30 +11%	0.23 −1%
MSG-RC15	29.07	6.49 −69%	10.02 −80%	44.55	−2.89 +21%	0.05 −1%	48.80	−1.19 +9%	0.09 −1%
Pleiades-Montpellier	22.31	4.67 −64%	7.48 −71%	36.30	−0.15 +1%	0.61 −4%	41.74	0.16 −1%	0.71 −3%
SFSI-Mantar-rad-rmnoise	39.60	4.95 −31%	9.26 −69%	53.98	−0.77 +7%	1.12 −11%	59.40	−1.50 +12%	0.60 −4%
SFSI-Mantar-raw	36.73	−0.13 +6%	0.23 −7%	40.03	−0.51 +8%	0.24 −3%	44.49	−1.06 +7%	0.04 −0%
SPOT5-Toulouse-1	23.47	−1.66 +29%	−0.09 +2%	28.48	−0.73 +6%	−0.06 +1%	33.16	−0.35 +3%	−0.04 +0%
VEGETATION-1-1c	34.42	−0.85 +7%	0.77 −7%	41.20	−0.46 +4%	0.06 −1%	45.92	−0.03 +0%	−0.12 +1%

Table 6.: Performance of the NLR rate-allocation method in comparison with the RW and PCRD methods, when employing the POT spectral transform and the Integer DWT spatial transform.

Image Name	1 bpppb			2 bpppb			3 bpppb		
	NLR (dB)	RW (Δ dB, %)	PCRD (Δ dB, %)	NLR (dB)	RW (Δ dB, %)	PCRD (Δ dB, %)	NLR (dB)	RW (Δ dB, %)	PCRD (Δ dB, %)
AIRS-Granule-9	56.93	0.07 −2%	0.42 −11%	60.34	−0.03 +0%	0.45 −8%	64.19	−0.20 +2%	0.02 −0%
AVIRIS-Hawaii-raw	45.47	0.35 −9%	0.63 −23%	49.11	0.02 −0%	0.66 −6%	57.18	−3.20 +13%	−0.14 +0%
AVIRIS-Yellowstone-rad	46.12	−0.53 +7%	0.57 −9%	50.41	0.44 −6%	0.71 −10%	54.47	0.30 −3%	0.48 −4%
AVIRIS-Yellowstone-raw	50.62	−0.43 +5%	0.59 −9%	55.26	0.07 −1%	0.54 −6%	59.82	−0.10 +1%	0.32 −2%
CASI-t0477f06-raw	40.49	0.19 −2%	2.22 −26%	47.35	−0.74 +8%	0.50 −6%	51.29	−0.63 +5%	0.38 −4%
CASI-t0477f06-raw-nuc	42.69	−1.62 +34%	0.66 −10%	47.86	−0.73 +9%	0.49 −7%	51.67	−0.52 +4%	0.46 −4%
CRISM-sc214-nuc	48.91	0.56 −5%	2.03 −29%	55.71	−0.31 +3%	0.69 −6%	60.54	−0.95 +7%	0.84 −3%
CRISM-sc214-raw	39.02	1.12 −10%	2.73 −20%	50.11	−1.96 +31%	0.65 −5%	55.48	−3.60 +17%	0.26 −2%
Hyperion-GeoSample-ff	24.65	0.19 −4%	0.61 −16%	28.08	0.15 −2%	0.40 −6%	32.30	−0.29 +2%	0.05 −0%
Hyperion-GeoSample-raw	42.67	0.27 −4%	1.39 −21%	48.50	−0.25 +3%	0.47 −6%	52.50	−0.22 +2%	0.24 −2%
Hyperion-Geo_Sample-nuc	46.04	0.03 −1%	0.57 −12%	50.07	0.05 −1%	0.32 −6%	54.19	−0.22 +2%	−0.07 +1%
IASI-Desert	45.99	0.11 −2%	1.10 −23%	50.69	−0.08 +1%	0.64 −9%	55.18	−0.39 +3%	0.21 −2%
Landsat-Coast	35.91	0.01 −1%	0.37 −17%	39.31	−0.61 +8%	0.04 −0%	48.19	−5.49 +44%	−0.82 +0%
Landsat-Mountain	26.53	−0.13 +2%	0.39 −4%	30.27	0.47 −6%	0.80 −4%	34.36	−0.14 +2%	−0.08 +1%
M3-M3globalA-nuc	54.10	−1.72 +28%	0.23 −5%	59.15	−0.95 +10%	0.03 −1%	66.06	−2.06 +10%	−0.13 +0%
M3-M3globalA-raw	41.86	−0.94 +8%	3.28 −27%	54.12	−1.58 +11%	0.27 −2%	59.57	−2.23 +19%	0.18 −2%
MODIS-250m-raw	23.61	11.30 −85%	12.68 −86%	43.74	−0.69 +3%	0.16 −2%	50.36	−0.61 +3%	0.15 −1%
MODIS-500m-raw	29.16	−1.36 +10%	0.82 −9%	36.03	0.98 −7%	2.15 −16%	38.76	4.53 −25%	5.75 −31%
MSG-RC15	32.15	5.98 −69%	8.02 −71%	45.65	−1.32 +14%	0.13 −0%	49.78	−0.03 +0%	0.54 −1%
Pleiades-Montpellier	29.10	0.17 −3%	0.30 −5%	36.36	−0.34 +2%	0.30 −2%	41.74	−0.03 +0%	0.41 −3%
SFSI-Mantar-rad-rmnoise	50.00	−1.24 +12%	0.61 −6%	56.22	−0.24 +2%	0.37 −3%	61.84	−1.00 +5%	0.82 −2%
SFSI-Mantar-raw	37.20	0.04 −2%	0.24 −8%	40.80	0.08 −1%	0.27 −4%	45.50	−0.30 +2%	−0.26 +2%
SPOT5-Toulouse-1	25.00	0.73 −13%	0.81 −14%	31.10	−0.09 +1%	0.10 −1%	35.48	−0.01 +0%	0.08 −1%
VEGETATION-1-1c	34.04	−0.32 +4%	1.91 −22%	41.87	−0.48 +4%	0.19 −2%	46.69	−0.26 +2%	−0.11 +1%

5. Conclusions

This article extends the rate-allocation method based on the NLR complexity, as described in Camarero, Delaunay, and Thiebaut (2012); Bru et al. (2011), to support unequal distortion weighting. Under unequal distortion weighting, the originally-available trivial solution is not applicable, and a new solution is devised by reformulating the rate functions as monotonically increasing functions of a common parameter. The proposed method is simple to implement and it is expected to be reasonably fast, without the need to modify CCSDS-122.0 implementations to yield accurate RD measurements. A practical rate-allocation algorithm is given.

Extensive experimental results are provided as well, showing that, under a

CCSDS-122.1 implementation, the proposed allocation method achieves low coding performances for low rates, while achieves coding performances similar to those obtainable by the quasi-optimal –but significantly more demanding of computational resources– PCRD allocation for high rates.

Acknowledgments

An earlier version of this work was presented in the ESA CNES On-Board Payload Data Compression Workshop 2016.

References

Akam Bita, Isidore Paul, Michel Barret, and Dinh-Tuan Pham. 2010. "On optimal orthogonal transforms at high bit-rates using only second order statistics in multicomponent image coding with JPEG2000." *Elsevier Signal Processing* 90 (3): 753 – 758.

Blanes, I., M. Hernandez-Cabronero, F. Auli-Llinas, J. Serra-Sagrista, and M.W. Marcellin. 2015. "Isorange Pairwise Orthogonal Transform." *Geoscience and Remote Sensing, IEEE Transactions on* 53 (6): 3361–3372.

Bru, Richard, Frédérique Ponchaut, Cindy Hortala, Pascal Prunet, Arnaud Ginestet, and Xavier Delaunay. 2011. *COMPRESSION À QUALITE FIXÉ - DÈBIT VARIABLE.* Tech. Rep. NOV-7031-NT-793. Noveltis.

Camarero, Roberto, Xavier Delaunay, and Carole Thiebaut. 2012. "Fixed-Quality/Variable bit-rate On-Board Image Compression for future CNES missions." *Proc. SPIE* 8514: 851402–851402–14.

Du, Qian, Nam Ly, and James E. Fowler. 2014. "An Operational Approach to PCA+JPEG2000 Compression of Hyperspectral Imagery." *IEEE Journal of Selected Topics in Applied Earth Observations and Remote Sensing* 7: 2237–2245.

Falzon, F., and S. Mallat. 1998. "Low bit rate image coding over bases." *Pattern Recognition, 1998. Proceedings. Fourteenth International Conference on* 2: 1260–1263.

Fowler, James E., and Justin T. Rucker. 2007. *Hyperspectral Data Exploitation: Theory and Applications.* chap. "3D wavelet-Based Compression of Hyperspectral Imager", 379–407. Hoboken, NJ, USA: John Wiley & Sons Inc.

Gall, D. Le, and A. Tabatabai. 1988. "Sub-band coding of digital images using symmetric short kernel filters and arithmetic coding techniques." *Proc. Int. Conf. Acoustics, Speech, and Signal Processing* 2: 761–764.

Gish, Herbert, and John N Pierce. 1968. "Asymptotically efficient quantizing." *Information Theory, IEEE Transactions on* 14 (5): 676–683.

Penna, B., T. Tillo, E. Magli, and G. Olmo. 2006a. "A New Low Complexity KLT for Lossy Hyperspectral Data Compression." *IGARSS 2006. IEEE International Conference on Geoscience and Remote Sensing Symposium, 2006.* 3525–3528.

Penna, Barbara, Tammam Tillo, Enrico Magli, and Gabriella Olmo. 2006b. "Progressive 3-D coding of hyperspectral images based on JPEG2000." *IEEE Geoscience and Remote Sensing Letters* 3 (1): 125–129.

Penna, Barbara, Tammam Tillo, Enrico Magli, and Gabriella Olmo. 2007. "Transform Coding Techniques for Lossy Hyperspectral Data Compression." *IEEE Transactions on Geoscience and Remote Sensing* 45 (5): 1408–1421.

Qian, S.E. 2013. *Optical Satellite Signal Processing and Enhancement.* SPIE.

Taubman, D.S., and M.W. Marcellin. 2002. *JPEG2000: Image Compression Fundamen-*

tals, Standards, and Practice. Vol. 642. Kluwer International Series in Engineering and Computer Science.

Zhang, J., J. E. Fowler, and G. Liu. 2008. "Lossy-to-Lossless Compression of Hyperspectral Imagery Using Three-Dimensional TCE and an Integer KLT." *IEEE Geoscience and Remote Sensing Letters* 5: 814–818.